ACS APPLIED MATERIALS & INTERFACES

Research Article

www.acsami.org

Modeling of Stresses and Strains during (De)Lithiation of Ni_3Sn_2-Coated Nickel Inverse-Opal Anodes

Hoon-Hwe Cho,*,† Matthew P. B. Glazer,‡ and David C. Dunand

Department of Materials Science and Engineering, Northwestern University, 2220 Campus Drive, Evanston, Illinois 60208, United States

Supporting Information

ABSTRACT: Tin alloy-based anodes supported by inverse-opal nanoscaffolds undergo large volume changes from (de)lithiation during cyclic battery (dis)charging, affecting their mechanical stability. We perform continuum mechanics-based simulation to study the evolution of internal stresses and strains as a function of the geometry of the active layer(s): (i) thickness of Ni_3Sn_2 single layer (30 and 60 nm) and (ii) stacking sequence of Ni_3Sn_2 and amorphous Si in bilayers (60 nm thick). For single Ni_3Sn_2 active layers, a thinner layer displays higher strains and stresses, which are relevant to mechanical stability, but causes lower strains and stresses in the Ni scaffold. For Ni_3Sn_2-Si bilayers, the stacking sequence significantly affects the deformation of the active layers and thus its mechanical stability due to different lithiation behaviors and volume changes.

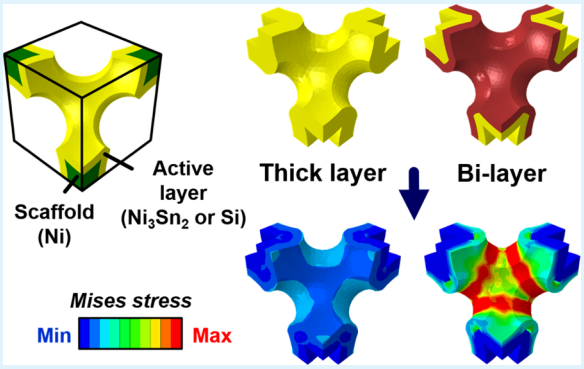

KEYWORDS: *tin anodes, lithiation strain, diffusion-stress coupling, active layer, stacking sequence*

1. INTRODUCTION

Lithium-ion batteries (LIBs) need to achieve significantly faster charging time and higher energy densities to increase their use in emerging and established applications such as automotive and electronic applications.[1−6] Tin alloy-based anodes are promising candidates for increasing both the power and energy density of LIBs as they exhibit a much higher capacity than that of conventionally utilized graphite (~994 vs 372 mAh/g).[7] However, these anodes exhibit a large volume expansion (~100%)[7−10] during lithiation, which can generate large stresses, thereby causing cracking, pulverization, and delamination in the anodes.[7] Reducing the dimensions and the relevant size scales of tin-based anode geometries is one strategy used to reduce the maximum stresses developed during lithiation;[7,11] however, there is limited understanding of the effect of scale and geometry of the anode upon the strains and stresses created by (de)lithiation-induced volume change. These strains and stresses affect mechanical stability, which is closely related to the resistance to irreversible processes, such as plasticity and fracture of these anodes during cyclic (dis)charging.

The evolution of internal stresses and strains and the resulting mechanical stability of tin- and the related silicon-based alloy anodes have been studied within the context of well-dispersed nanocrystals subjected to lithiation by employing theoretical and experimental approaches.[12−14] Furthermore, we recently studied the mechanical behavior of a Si active layer deposited on a Ni scaffold during (de)lithiation by employing finite element (FE) modeling.[15] Here, we carry out a study of the evolution of internal stresses and strains as a function of geometrical parameters by considering two cases: (i) a Ni_3Sn_2 single layer with two different thicknesses and (ii) a bilayer consisting of a Ni_3Sn_2 and an amorphous Si layer, where the coating sequence is varied. Specifically, we build upon our previous study[15] of a silicon-coated nickel inverse-opal anode and employ sequentially-coupled stress and diffusion FE modeling to predict the internal stresses and strains of an anode system consisting of Ni_3Sn_2 coated on a nickel inverse-opal substrate. The predicted strain values in the Ni substrate are then compared with those measured in operando via synchrotron X-ray diffraction, using the Ni-average lattice crystallographic spacings. On the basis of this validation of the FE model, we then compute the effect of thickness of the active Ni_3Sn_2 layer on the stress and strain evolution during cyclic (dis)charging. Additionally, we investigate the case of an active bilayer consisting of Ni_3Sn_2 and amorphous Si, and we compare plastic strains to those calculated for a single active layer for Ni_3Sn_2 of the same thickness.

2. RESULTS AND DISCUSSION

For the FE simulations used here, we adopt the hard contact condition to describe the interactions between the two phases (Ni_3Sn_2 and Ni) in the anode[15] (the governing equations and boundary conditions are presented in the Supporting Information). This computational framework has been used

Received: February 3, 2017
Accepted: April 19, 2017
Published: April 19, 2017

DOI: 10.1021/acsami.7b01640
ACS Appl. Mater. Interfaces 2017, 9, 15433−15438

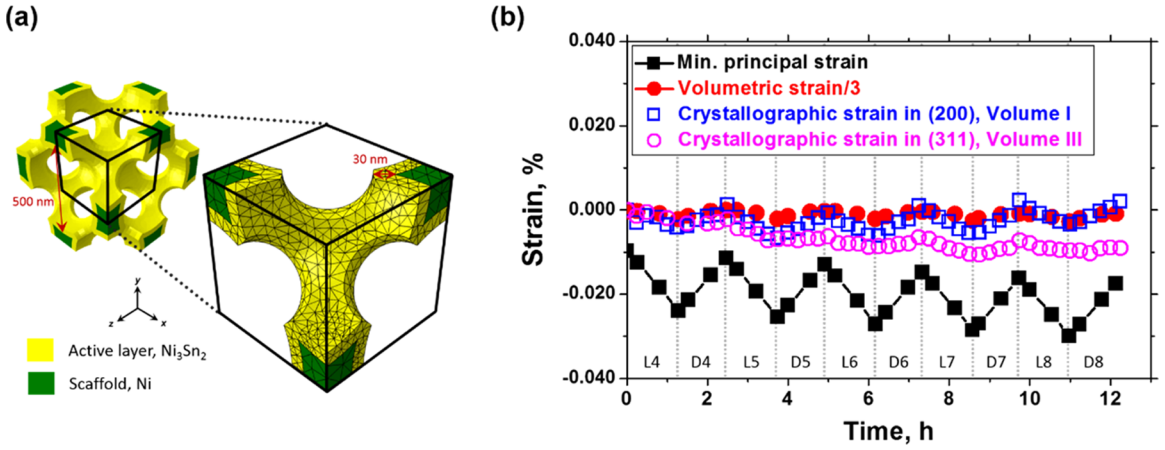

Figure 1. (a) Three-dimensional (3D) mesh structure of the RVE for a Ni inverse-opal electrode coated with a 30 nm thick Ni_3Sn_2 active layer (thin layer). The Ni_3Sn_2 and Ni structures have 9063 and 696 tetrahedral elements, respectively. (b) Comparison of the computed and measured strain evolution in the Ni scaffold over five lithiation−delithiation cycles (marked L and D) starting from the fourth cycle. The two solid lines indicate the computed strains (the black and red lines correspond to the minimum principal strain and one-third of the volumetric strain, respectively); the hollow symbols represent measured strain data: in-plane average crystallographic strains measured from Ni (200) and (311) diffraction peaks (blue square and magenta circle, for two different volumes in the same specimens, labeled I and III) to illustrate reproducibility. The sizes of the symbols for the experimental data are larger than the uncertainty of the measured strains.

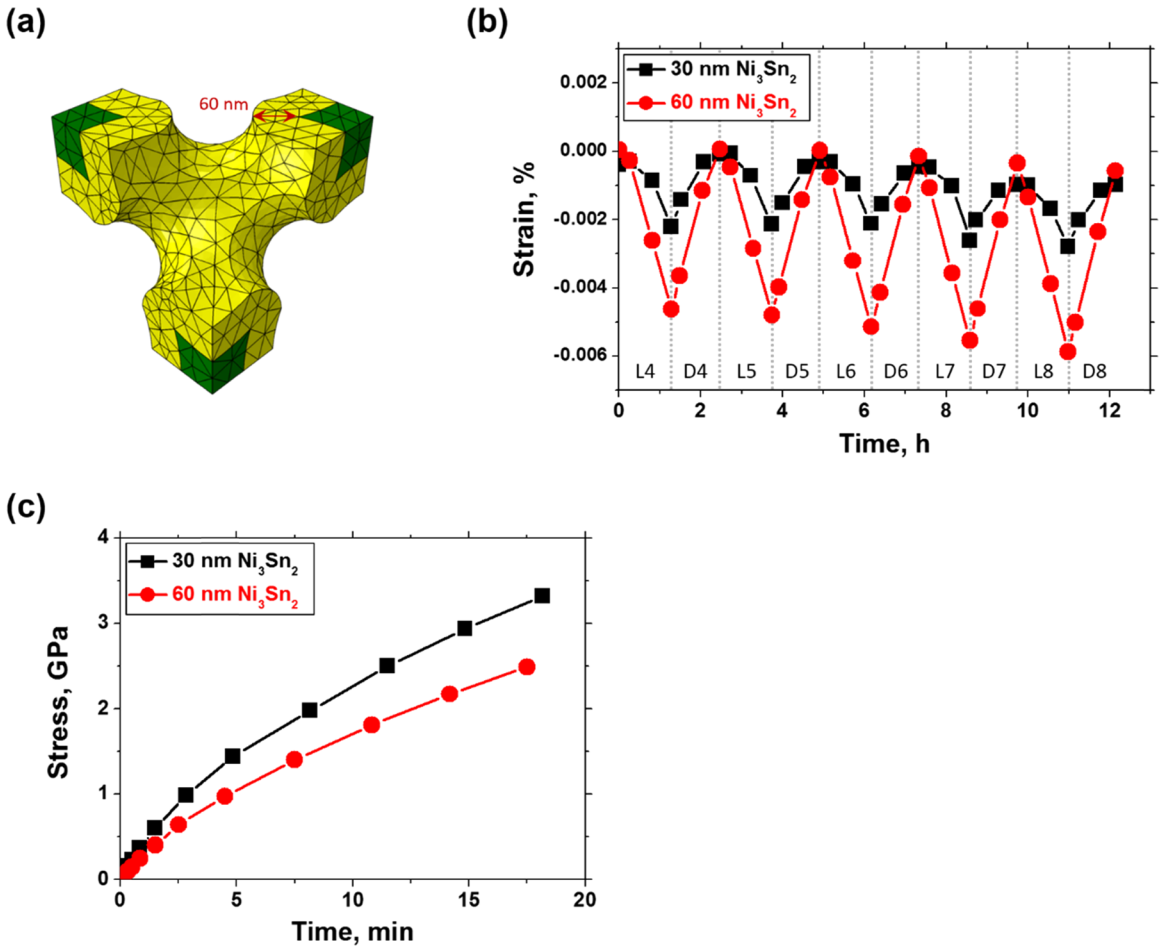

Figure 2. (a) Three-dimensional mesh structure of the RVE with a 60 nm Ni_3Sn_2 active layer (thick layer). (b) Comparison of the computed compressive strain evolution developed in Ni due to volume change of the 30 and 60 nm thick active layers for five (de)lithiation cycles, starting after the third lithiation−delithiation cycle. The black and red lines correspond to one-third of the volume average of the volumetric strains computed from the thin and thick active layers, respectively. (c) Comparison of the computed maximum von Mises stress (averaged over the 10% of elements with the highest von Mises value) time evolution in thin and thick Ni_3Sn_2 active layers during a part of the first lithiation half-cycle.

DOI: 10.1021/acsami.7b01640
ACS Appl. Mater. Interfaces 2017, 9, 15433−15438

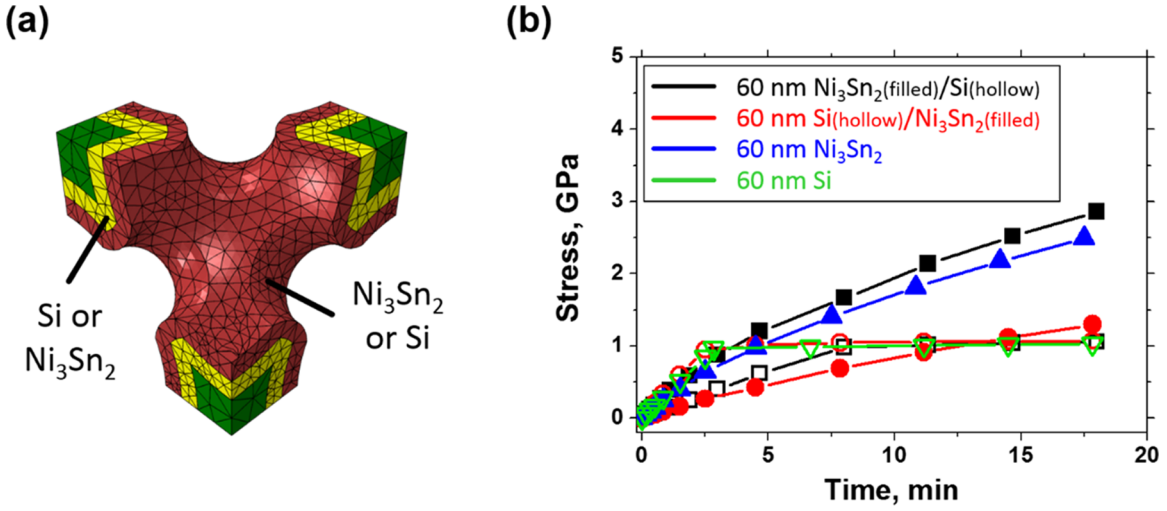

Figure 3. (a) Three-dimensional mesh systems of the RVE having thick active bilayers. Each active layer with 30 nm thickness can be either Ni_3Sn_2 or amorphous Si. (b) Comparison of the computed maximum von Mises stress (averaged over the 10% of elements with the highest von Mises values) evolutions in each of the layers of the bilayers: Si/Ni_3Sn_2 (where Si is the outer layer) and Ni_3Sn_2/Si (where Si is the inner layer) during the first lithiation half-cycle. For comparison, the computed maximum von Mises stress evolutions in the single layer cases are also shown.

and proven to be reliable to reproduce the internal strains observed experimentally in similar silicon-coated nickel inverse-opal anodes during cycling.[15] We first create a representative volume element (RVE) of the Ni_3Sn_2-coated nickel inverse-opal anode, as illustrated in Figure 1a. The RVE comprises the Ni_3Sn_2 active layer and the Ni scaffold, where the surface between these phases are in contact. The thickness of the active layer is 30 nm, and the Ni scaffold has a pore size of 500 nm. Tetrahedral elements (C3D10T) were used for all models. Ni_3Sn_2 and Ni have 9063 and 696 elements, respectively, as illustrated in Figure 1a. Mesh sensitivity analysis was carried out for the first lithiation, varying from 9063 to 13 078 (Ni_3Sn_2 element number) and from 696 to 1178 (Ni element number). For the element numbers used in the rest of this study, sensitivity was negligible. The RVE has an open porosity of 50% of the total volume, and the solid volume fractions of the Ni scaffold and Ni_3Sn_2 active layer are 26 and 24%, respectively. Figure 1b shows strain evolutions developed in Ni due to the lithiation-induced volume change of Ni_3Sn_2 (which are discussed in detail in the Supporting Information) during five (dis)charging cycles. The black line corresponds to the volume average of the minimum principal strain computed from each element, and the blue line corresponds to one-third of the volume average of the volumetric strain computed from each element. The latter strain is expected to be directly comparable to the strain data measured from X-ray diffraction. The in-plane average crystallographic strains, previously measured in a Ni_3Sn_2-coated Ni scaffold with the same geometry,[10] are also shown in Figure 1b for the Ni (200) and (311) diffraction patterns on five (dis)charging cycles. There is reasonable quantitative agreement between the computed and measured strain data. Li ions diffuse into the active layer during lithiation, leading to a free expansion toward the pore volume, whereas the Ni scaffold prevents expansion toward the scaffold. This resistance to the expansion of the active layer causes net average compression in the Ni scaffold, and the compressive strain increases linearly with the degree of lithiation, as shown in Figure 1b. The differences in stiffness between these two crystallographic orientations (approximately 137 GPa in (200) and 217 GPa in (311))[16] causes the difference in the slope between the compressive strains and the corresponding magnitude of those. The computed compressive strain at the fourth full lithiation point (labeled L4 in Figure 1b) is −0.00222%, which is similar to the measured value of −0.00241% collected from X-ray diffraction. The compressive strain recovers rapidly during the subsequent delithiation, which results in a fully recovered strain after the fourth lithiation−delithiation cycle.

We then examine how the thickness of the active layer affects the internal stresses and strains and creates an RVE with a 60 nm thick active layer (i.e., twice the thin 30 nm thickness in Figure 1b), as illustrated in Figure 2a. Ni_3Sn_2 and Ni have 8789 and 696 elements, respectively. The RVE has an open porosity of 22% of the total volume, and the solid volume fractions of the Ni scaffold and Ni_3Sn_2 active layer are 26 and 52%, respectively. Figure 2b shows the computed compressive strain evolution during five (de)lithiation cycles developed in the Ni scaffold due to the lithiation-induced volume change of the Ni_3Sn_2 active layers with 30 and 60 nm thickness. The slopes of the strain curves are nearly linear through the (de)lithiation process in both cases, indicating that plastic deformation or yielding does not occur in the Ni scaffold. During the five cycles, compressive strains in both cases accumulate gradually in the Ni scaffold after each cycle. The computed compressive strains of the Ni scaffold with a thicker (60 nm) active layer after each full lithiation are −0.0046, −0.0048, −0.0051, −0.0055, and −0.0059%, respectively, which are approximately twice the computed values of −0.0022, −0.0021, −0.0021, −0.0026, and −0.0028% of the Ni scaffold having a thinner (30 nm) active layer, respectively.

To further explore the effect of the active layer thickness on the mechanical stability of the anode, the computed maximum von Mises stress is plotted as a function of lithiation time during the first 18 min of lithiation (corresponding to 23% of full lithiation) for the two cases with different thickness, as seen in Figure 2c. The maximum stress is defined as the averaged stress in 10% of elements that show the highest von Mises stress, which can be used as a criterion to determine mechanical stability of the active layer.[17−19] Stress accumulation in the thin active layer occurs faster than that in the thick active layer,

DOI: 10.1021/acsami.7b01640
ACS Appl. Mater. Interfaces 2017, 9, 15433−15438

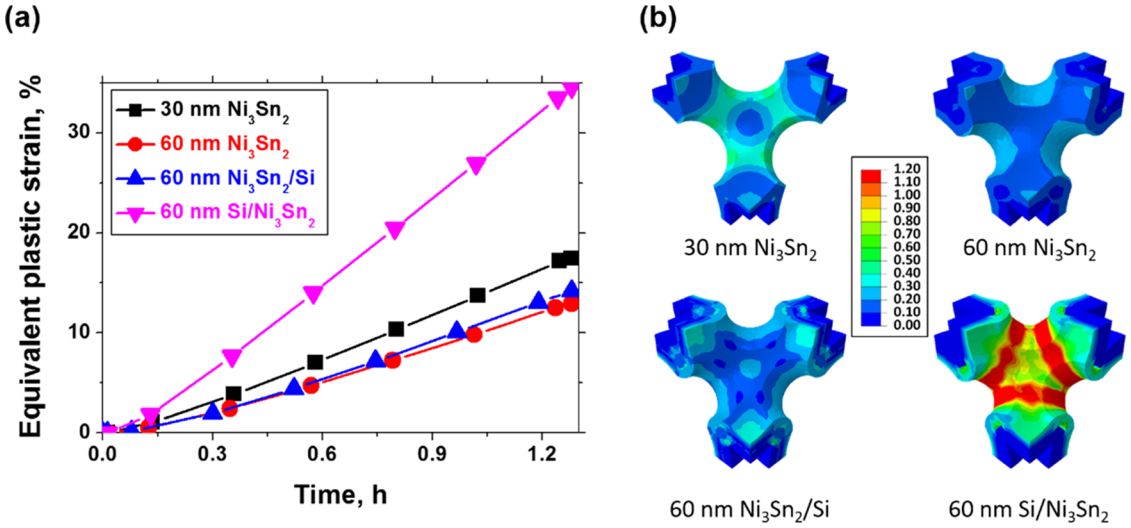

Figure 4. (a) Computed equivalent plastic strain evolutions in the active layers for four cases (30 nm Ni_3Sn_2, 60 nm Ni_3Sn_2, 60 nm Ni_3Sn_2/Si, and 60 nm Si/Ni_3Sn_2) during the first lithiation half-cycle. The black, red, blue, and magenta lines correspond to volume-averaged von Mises (equivalent) plastic strains computed for the thin Ni_3Sn_2, thick Ni_3Sn_2, thick Si/Ni_3Sn_2 (Si outer layer), and thick Ni_3Sn_2/Si (Si inner layer) cases, respectively. (b) Computed equivalent plastic strain distributions of the active layers of four cases at the full lithiation state with the color contours corresponding to surfaces of equivalent strains (unitless).

indicating that the thin layer is more affected by the constrained volumetric expansion during lithiation, despite the lower stains developed in the Ni scaffold on which the thin active layer is deposited. This indicates that increasing the thickness and the corresponding higher solid volume fraction of the active layer raises its mechanical stability against volumetric expansion, leading to less strain transfer in the active layer.[20] Therefore, the insight (i.e., thinner active layer is mechanically less stable but causes smaller strains in the scaffold) gained here by studying the effect of two active layer thicknesses may serve, when further confirmed computationally and experimentally, as a pathfinder in devising practical anodes customized for superior mechanical properties.

We turn now to the design of a novel electrode, where the single active layer is replaced by an active bilayer of the same 60 nm thickness, consisting of Ni_3Sn_2 and amorphous silicon, as seen in Figure 3a. Two cases are considered: (i) Ni_3Sn_2/Si, where the outer active layer is Ni_3Sn_2 and the inner layer is amorphous Si; (ii) Si/Ni_3Sn_2, where the outer and inner layers are Si and Ni_3Sn_2, respectively. The inner and outer layers and the Ni scaffold have 9063, 9711, and 696 tetrahedral elements, respectively. The solid volume fractions of the outer and inner active layers are 28 and 24%, respectively, with the solid volume fraction of the Ni scaffold (26%) and open porosity occupying the rest (22%) of the volume. The diffusivity of Li in Ni_3Sn_2 is one-third of that in Si,[7,9] thus causing slower diffusion of Li in the Ni_3Sn_2 active layer. Also, the volumetric expansion of Ni_3Sn_2 with Li concentration (0.22 m^3/mol)[15] is approximately one fourth of that in Si (0.82 m^3/mol),[21] thus causing strain incompatibilities between the two layers. Figure 3b shows the computed maximum von Mises stress in each of the two layers for the above two cases during the first 18 min of the lithiation process. As seen in Figure 3b, stress accumulation in the outer layers is steeper than that in the inner layer. In both cases, the outer layers have a higher lithium concentration than that of the inner layers during lithiation, leading to a faster lithiation-induced volume change in the outer layer, thereby increasing internal stresses of the outer layer. Volumetric expansion coefficients of Ni_3Sn_2 and Si with Li concentration affect the mechanical stability of each active layer, indicating that the stress accumulation of Si is different from that of Ni_3Sn_2 at the same layer due to different lithiation-induced volume expansion. Figure 3b also shows the computed maximum von Mises stress in single layers (Si or Ni_3Sn_2), with the same 60 nm thickness. As seen in Figure 3b, bilayers increase the maximum von Mises stress of the outer layer slightly, as compared to that of single layers with the same total thickness, whereas stress accumulation in the single layers is steeper than that in the inner layers of bilayers due to slower diffusion of Li into the inner layer. Additionally, stress accumulation of the thick Si layer is slightly steeper than that in the thick Ni_3Sn_2 layer up to the onset of the plateau region upon yielding of Si due to larger lithiation-induced volume expansion of Si (and thus incompatibility with Ni). After the onset of the plateau region of Si, stress accumulation of the thick Ni_3Sn_2 layer increases continuously up to the onset of plateau region of Ni_3Sn_2, whereas stress accumulation of the thick Si layer shows the plateau region due to different stress−strain curves of Ni_3Sn_2 and Si, as seen in Figure S3 and ref 15.

To compare the four cases studied here (the two Ni_3Sn_2 single layers, and the two 60 nm bilayers), the volume averages of von Mises (equivalent) plastic strains computed from each element in the active layers are averaged and plotted as a function of the lithiation time, as shown in Figure 4a. These four cases show a similar onset of plasticity, indicating that yielding in the active layer begins at approximately 0.15 h in all cases. However, the four cases exhibit significantly different rates of increase of volume-averaged equivalent plastic strain, demonstrating that the geometrical modification of the active layer significantly affects the mechanical state of the active layer. The plastic strain accumulation of the Ni_3Sn_2-Si bilayer is the steepest, indicating that this configuration is the most unstable (among the four cases studied here) against lithiation-induced volume expansion. The plastic strain accumulation of the thin layer is steeper than that of the thick layer. Thus, the plastic strain accumulation is sensitive to the thickness, number, and stacking sequence of the active layer. Figure 4b shows the computed equivalent plastic strain distributions of the active

DOI: 10.1021/acsami.7b01640
ACS Appl. Mater. Interfaces 2017, 9, 15433−15438

layers of the four cases after the first lithiation half-cycle (1.28 h). The computed equivalent plastic strain distribution in the inner layer of the bilayer is discussed in detail in the Supporting Information. Each of the four cases shows a different plastic strain distribution, with plastic strain concentrated at some regions (struts) of each active layer where mechanical damage and cracking are thus most likely to occur. Among the four cases, the thick Ni_3Sn_2 and the Ni_3Sn_2/Si cases have a nearly similar plastic strain distribution at the full lithiation state as seen in the evolution of plastic strain in Figure 4a. In the Ni_3Sn_2/Si case, the inner layer Si appears to not significantly affect the plastic strain distribution and profile of the outer Ni_3Sn_2 layer. By contrast, the Si/Ni_3Sn_2 case has the severest strain concentration (Figure 4b), which is in agreement with the steepest plastic strain evolution (Figure 4a). These findings indicate that the plastic properties of the outer layer could determine its elastoplastic behavior during lithiation-induced volume expansion regardless of the inner layer.

3. SUMMARY

In summary, continuum mechanics-based simulations were carried out to study the geometrical effect on the stress and strain evolution of Ni_3Sn_2-coated Ni scaffolds subjected to (de)lithiation. In particular, modifying the geometry of the active layer affects the evolution of internal stresses and strains in both the active layer and scaffold. First, the evolution during (de)lithiation of the volume average of the compressive strain computed in the Ni scaffold agrees with experimental measurements based on in operando synchrotron X-ray diffraction. Second, plastic deformation or yielding does not seem to develop in the Ni scaffold due to linearity of the slopes of the strain versus time curves through the (de)lithiation process. Also, an increase of thickness of the active layer leads to an increase of the strains developed in the Ni scaffold but decreases strains in the active layer, thus raising its mechanical stability against the volumetric expansion due to its higher solid volume fraction. Additionally, a thick Ni_3Sn_2/Si layer increases the plastic strain of the outer layer slightly, as compared with a thick Ni_3Sn_2 layer with the same total thickness. Finally, the stacking sequence of the Ni_3Sn_2 and Si active layers affects the plastic strain of the active layers (and thus their mechanical stability) due to different lithiation kinetics and volume change.

■ ASSOCIATED CONTENT

Supporting Information

The Supporting Information is available free of charge on the ACS Publications website at DOI: 10.1021/acsami.7b01640.

Details of governing equations and boundary conditions; volumetric expansion of Ni_3Sn_2 during lithiation; hydrostatic stress effect on the diffusion flux; hard contact behavior between the contacted surfaces; stress−strain curves of Ni_3Sn_2 and Ni, Li, concentration and corresponding volumetric strain evolutions computed in Ni_3Sn_2 active layer after third lithiation−delithiation cycle; equivalent plastic strain distributions of inner and outer layers of bilayer structures at the full lithiation state; strain analysis methods of XRD data; electrode fabrication; electrochemical measurements (PDF)

■ AUTHOR INFORMATION

Corresponding Author

*E-mail: hhcho@hanbat.ac.kr.

ORCID

Hoon-Hwe Cho: 0000-0002-9815-3739

Present Addresses

‡Materials and Corrosion Engineering Practice, Exponent, Inc.,149 Commonwealth Drive, Menlo Park, California 94025, United States (M.P.B.G.).

†Department of Materials Science and Engineering, Hanbat National University, Daejeon, South Korea (H.-H.C).

Notes

The authors declare no competing financial interest.

■ ACKNOWLEDGMENTS

This research was supported by the newly appointed professor research fund of Hanbat National University in 2016. The authors thank Prof. Paul V. Braun (University of Illinois at Urbana−Champaign) for useful discussions.

■ REFERENCES

(1) Tarascon, J. M.; Armand, M. Issues and Challenges Facing Rechargeable Lithium Batteries. *Nature* **2001**, *414*, 359−367.

(2) Arthur, T. S.; Bates, D. J.; Cirigliano, N.; Johnson, D. C.; Malati, P.; Mosby, J. M.; Perre, E.; Rawls, M. T.; Prieto, A. L.; Dunn, B. Three-Dimensional Electrodes and Battery Architectures. *MRS Bull.* **2011**, *36*, 523−531.

(3) Whittingham, M. S. History, Evolution, and Future Status of Energy Storage. *Proc. IEEE* **2012**, *100*, 1518−1534.

(4) Amine, K.; Kanno, R.; Tzeng, Y. H. Rechargeable Lithium Batteries and Beyond: Progress, Challenges, and Future Directions. *MRS Bull.* **2014**, *39*, 395−405.

(5) Li, X.; Gu, M.; Hu, S. Y.; Kennard, R.; Yan, P. F.; Chen, X. L.; Wang, C. M.; Sailor, M. J.; Zhang, J. G.; Liu, J. Mesoporous Silicon Sponge as an Anti-Pulverization Structure for High-Performance Lithium-Ion Battery Anodes. *Nat. Commun.* **2014**, *5*, No. 4105.

(6) Larcher, D.; Beattie, S.; Morcrette, M.; Edström, K.; Jumasc, J. C.; Tarascon, J. M. Recent Findings and Prospects in the Field of Pure Metals as Negative Electrodes for Li-Ion Batteries. *J. Mater. Chem.* **2007**, *17*, 3759−3772.

(7) Zhang, W. J. A Review of the Electrochemical Performance of Alloy Anodes for Lithium-Ion Batteries. *J. Power Sources* **2011**, *196*, 13−24.

(8) Zhang, H.; Shi, T.; Wetzel, D. J.; Nuzzo, R. G.; Braun, P. V. 3D Scaffolded Nickel-Tin Li-Ion Anodes with Enhanced Cyclability. *Adv. Mater.* **2016**, *28*, 742−747.

(9) Zhang, W. J. Lithium Insertion/Extraction Mechanism in Alloy Anodes for Lithium-Ion Batteries. *J. Power Sources* **2011**, *196*, 877−885.

(10) Glazer, M. P. B.; Wang, J.; Cho, J.; Puente, A. P. y.; Sauza, D. J.; Okasinski, J.; Almer, J.; Braun, P. V.; Dunand, D. C. Measuring Strain In Operando by X-Ray Diffraction in Bicontinuous Si and Nisn Inverse Opal Anodes under Rapid Cycling Conditions. *Electrochem. Soc.* **2015**, *2*, 265.

(11) Song, M. K.; Park, S.; Alamgir, F. M.; Cho, J.; Liu, M. L. Nanostructured Electrodes for Lithium-Ion and Lithium-Air Batteries: the Latest Developments, Challenges, and Perspectives. *Mater. Sci. Eng., R* **2011**, *72*, 203−252.

(12) Kim, H.; Seo, M.; Park, M. H.; Cho, J. A Critical Size of Silicon Nano-Anodes for Lithium Rechargeable Batteries. *Angew. Chem., Int. Ed.* **2010**, *49*, 2146−2149.

(13) Aifantis, K. E.; Hackney, S. A. Mechanical Stability for Nanostructured Sn- and Si-Based Anodes. *J. Power Sources* **2011**, *196*, 2122−2127.

(14) Liu, X. H.; Zhong, L.; Huang, S.; Mao, S. X.; Zhu, T.; Huang, J. Y. Size-Dependent Fracture of Silicon Nanoparticles During Lithiation. *ACS Nano* **2012**, *6*, 1522−1531.

(15) Cho, H. H.; Glazer, M. P. B.; Xu, Q.; Han, H. N.; Dunand, D. C. Numerical and Experimental Investigation of (De)Lithiation-Induced

DOI: 10.1021/acsami.7b01640
ACS Appl. Mater. Interfaces 2017, 9, 15433−15438

Strains in Bicontinuous Silicon-Coated Nickel Inverse Opal Anodes. *Acta Mater.* **2016**, *107*, 289−297.
(16) Courtney, T. H. *Mechanical Behavior of Materials*, 2nd ed.; McGraw Hill: Boston, 2000; p xviii.
(17) Cho, Y.; Ahn, T. H.; Cho, H. H.; Shin, J. H.; Moon, J. H.; Yang, S.; Choi, I. S.; Han, H. N.; Li, J. Study of Architectural Responses of 3D Periodic Cellular Materials. *Modell. Simul. Mater. Sci. Eng.* **2013**, *21*, No. 065018.
(18) Cho, H. H.; Cho, Y.; Han, H. N. Finite Element Analysis for Mechanical Response of Ti Foams with Regular Structure Obtained by Selective Laser Melting. *Acta Mater.* **2015**, *97*, 199−206.
(19) Cho, H. H.; Chen-Wiegart, Y. C. K.; Dunand, D. C. Finite Element Analysis of Mechanical Stability of Coarsened Nanoporous Gold. *Scr. Mater.* **2016**, *115*, 96−99.
(20) Gibson, L. J.; Ashby, M. F. *Cellular Solids: Structure and Properties*, 2nd ed.; Cambridge University Press: Cambridge, New York, 1997; p xviii.
(21) Obrovac, M. N.; Christensen, L.; Le, D. B.; Dahnb, J. R. Alloy Design for Lithium-Ion Battery Anodes. *J. Electrochem. Soc.* **2007**, *154*, A849−A855.

DOI: 10.1021/acsami.7b01640
ACS Appl. Mater. Interfaces 2017, 9, 15433−15438